Novel Multistatic Adaptive Microwave Imaging Methods for Early Breast Cancer Detection

Yao Xie,[1] Bin Guo,[1] Jian Li,[1] and Petre Stoica[2]

[1] Department of Electrical and Computer Engineering, University of Florida, P.O. Box 116200, Gainesville, FL 32611-6200, USA
[2] Systems and Control Division, Department of Information Technology, Uppsala University, P.O. Box 337, 75105 Uppsala, Sweden

Multistatic adaptive microwave imaging (MAMI) methods are presented and compared for early breast cancer detection. Due to the significant contrast between the dielectric properties of normal and malignant breast tissues, developing microwave imaging techniques for early breast cancer detection has attracted much interest lately. MAMI is one of the microwave imaging modalities and employs multiple antennas that take turns to transmit ultra-wideband (UWB) pulses while all antennas are used to receive the reflected signals. MAMI can be considered as a special case of the multi-input multi-output (MIMO) radar with the multiple transmitted waveforms being either UWB pulses or zeros. Since the UWB pulses transmitted by different antennas are displaced in time, the multiple transmitted waveforms are orthogonal to each other. The challenge to microwave imaging is to improve resolution and suppress strong interferences caused by the breast skin, nipple, and so forth. The MAMI methods we investigate herein utilize the data-adaptive robust Capon beamformer (RCB) to achieve high resolution and interference suppression. We will demonstrate the effectiveness of our proposed methods for breast cancer detection via numerical examples with data simulated using the finite-difference time-domain method based on a 3D realistic breast model.

1. INTRODUCTION

Breast cancer takes a tremendous toll on our society. One in eight women in the US will get breast cancer in her lifetime [1]. Each year more than 200 000 new cases of invasive breast cancer are diagnosed and more than 40 000 women die from the disease in the US alone [1]. Early diagnosis is currently the best hope of surviving breast cancer.

Currently, X-ray mammography is the standard routine breast cancer screening tool. However, the effectiveness of X-ray mammography has been questioned by certain sources in recent years and is somewhat currently under debate due to its inherent limitations in resolving both low- and high-contrast lesions and masses in radiologically dense glandular breast tissues. Breast tissues of younger women typically present a higher ratio of dense to fatty tissues, limiting the effectiveness of X-ray mammography. Hence mammography presents its major limitation in the sector of the population of highest public health interest and criticality. Some techniques such as magnetic resonance imaging (MRI) and Positron emission tomography (PET) have led to an increase in the identification of small abnormalities in the human breast, but the widespread use of MRI and PET for routine breast cancer screening is unlikely due to their high costs.

Ultra-wideband (UWB) confocal microwave imaging (CMI) is one of the most promising and attractive new screening technologies currently under development: it is nonionizing (safe), noninvasive (comfortable), sensitive (to tumors), specific (to cancers), and low-cost [2]. Its physical basis lies in the significant contrast in the dielectric properties between normal and malignant breast tissues [3–7]. In CMI, UWB pulses are transmitted from antennas at different locations near the breast surface and the backscattered responses from the breast are recorded, from which the image of the backscattered energy distribution is reconstructed coherently.

The data acquisition approaches and the associated signal processing methods affect the CMI imaging quality. There are three major data acquisition schemes: monostatic [8], bistatic [9, 10], and multistatic [11]. For monostatic CMI, the transmitter is also used as a receiver and is moved across the breast to form a synthetic aperture. For bistatic CMI, one transmitting and one receiving antenna are used as a pair and moved across the breast to form a synthetic aperture. For multistatic CMI, a real aperture array (see Figure 1) is used for data collection. Each antenna in the array takes turns to transmit a probing pulse, and all antennas (in some cases, all except the transmitting antenna) are used to receive
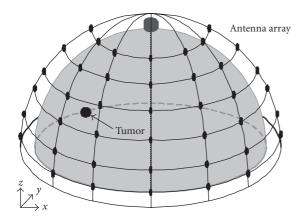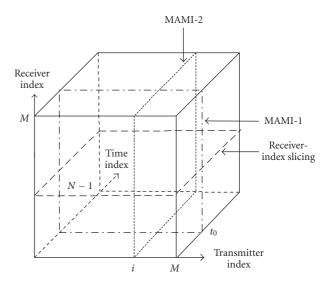
Figure 1: Antenna array configuration.

Figure 2: Multistatic CMI data cube model. In Stage I, MAMI-1 slices the data cube for each time index, whereas MAMI-2 slices the data cube for each transmitter index. Then RCB is applied to each data slice to obtain multiple waveform estimates.

the backscattered signals. Multistatic CMI can be considered as a special case of the wideband multi-input multi-output (MIMO) radar [12–14] with the multiple transmitted waveforms being either UWB pulses or zeros. Since the UWB pulses transmitted by different antennas are displaced in time, the multiple transmitted waveforms are orthogonal to each other. The monostatic and bistatic schemes exploit the transmitter spatial diversity, and the multistatic scheme takes advantage of the transmitter-and-receiver spatial diversity. The multistatic approach can give better imaging results than its mono- or bistatic counterparts when the synthetic aperture formed by the latter two approaches is similar to the real aperture array used by the former. An intuitive explanation would be that the multistatic approach utilizes the receiver diversity as well, by simultaneously recording multiple received signals that propagate via different routes and hence accrues more information about the tumor.

The challenge to CMI imaging is to devise signal processing algorithms to improve resolution and suppress strong interferences caused by the breast skin, nipple, and so forth. Signal processing algorithms can be classified as data-dependent (data-adaptive) and data-independent methods. For mono- and bistatic ultra-wideband CMI, the simple data-independent delay-and-sum (DAS) [8, 11], the data-independent microwave imaging space-time (MIST) beamforming [15], the data-adaptive robust Capon beamforming (RCB) [9, 10], as well as the data-adaptive amplitude and phase estimation (APES) [9, 10] methods have been considered for image formation. For multistatic ultra-wideband CMI, the DAS- [11] and RCB-based adaptive [16] methods have been considered. The data-adaptive methods can have better resolution and much better interference suppression capability and can significantly outperform their data-independent counterparts.

In this paper, we consider multistatic adaptive microwave imaging (MAMI) methods to form images of the backscattered energy for early breast cancer detection. For a location of interest (or focal point) $\mathbf{r}$ within the breast, the complete recorded multistatic data can be represented by a cube, as shown in Figure 2. In [16], we proposed a MAMI approach,

referred to MAMI-1 herein, which is a two-stage time-domain signal processing algorithm for multistatic CMI. In Stage I, MAMI-1 slices the data cube corresponding to each time index, and processes the data slice by the robust Capon beamformer (RCB) [17–19] to obtain backscattered waveform estimates at each time instant. Based on these estimates, in Stage II a scalar waveform is retrieved via RCB, the energy of which is used as an estimate of the backscattered energy for the focal point. MAMI-1 has been shown to have better performance than other existing methods. An alternative way of slicing the data cube in Stage I before applying RCB is to select a slice corresponding to each transmitting antenna index (see Figure 2). The so-obtained approach is referred to as MAMI-2 herein. We will show that MAMI-2 tends to yield better images than MAMI-1 for high input signal-to-interference-noise ratio (SINR), but worse images at low SINR. We will also show that combining MAMI-1 and MAMI-2 yields good performance in all cases of SINR. We refer to the combined method as MAMI-C herein.

We will demonstrate the performance of the MAMI methods using data simulated with the finite difference time domain (FDTD) method. The simulated breast models considered in the literature include a two-dimensional (2D) model based on a breast MRI scan [8, 15], simple three-dimensional (3D) and planar models [20], and the more realistic 3D model [9, 10, 21]. Our simulations are based on the 3D hemispherical breast model. The tumor response for the realistic 3D model is much smaller than that for the 2D (or 3D cylindrical) model due to tumor being assumed infinitely long in the latter model. The MAMI methods can detect tumors as small as 4 mm in diameter based on the realistic 3D model. Based on 2D models, the MAMI methods can detect tumors as small as 1.5 mm in diameter. We have only

included the realistic 3D-model-based examples herein since the conclusions drawn from 2D based models are similar.

The following notation will be used: $(\cdot)^T$ denotes the transpose, $\mathcal{R}^{m \times n}$ stands for the Euclidean space of dimension $m \times n$, $\mathbf{B} \succeq 0$ means that $\mathbf{B}$ is positive semidefinite, bold lowercase symbols represent vectors, and bold capital letters represent matrices.

2. DATA MODEL

We consider a multistatic imaging system, where K antennas are arranged on a hemisphere relatively close to the breast skin, at known locations. The configuration of the array is shown in Figure 1. The antennas are arranged on P layers with Q antennas per layer, where $K = PQ$. Each antenna takes turns to transmit an UWB probing pulse while all of the antennas are used to record the backscattered signals. Let $x_{i,j}(t)$, $i = 1, \ldots, K$, $j = 1, \ldots, K$, $t = 0, \ldots, N-1$, denote the backscattered signal generated by the probing pulse sent by the ith transmitting antenna and received by the jth receiving antenna, where t denotes the time sample. The 3×1 vector $\mathbf{r}$ denotes the focal point (i.e., an imaging location within the breast). In our algorithms, the location $\mathbf{r}$ is varied to cover all grid points of the breast model.

Our goal is to form a 3D image of the backscattered energy $E(\mathbf{r})$ on a grid of points within the breast, with the scope of detecting the tumor. The backscattered energy is estimated from the complete received data $\{x_{i,j}(t)\}$ for each location $\mathbf{r}$ of interest.

Before image formation, we preprocess the received signals $\{x_{i,j}(t)\}$ to remove, as much as possible, backscattered signals other than the tumor response, to align all the recorded signals from $\mathbf{r}$ by time-shifting, and to compensate for the propagation loss of the signal amplitude. (See [16] for details.) The preprocessed signals $y_{i,j}(t)$ obtained from $x_{i,j}(t)$ can be described as

$$y_{i,j}(t) = s_{i,j}(t) + e_{i,j}(t), \quad i, j = 1, \ldots, K, \ t = 0, \ldots, N-1, \tag{1}$$

where $s_{i,j}(t)$ represents the tumor response and $e_{i,j}(t)$ represents the residual term. The residual term $e_{i,j}(t)$ includes the thermal noise and the interference due to undesired reflections from the breast skin, nipple, and so forth. To cast (1) in a form suitable for the application of RCB [17], we approximate the data model (1) by making different assumptions. In the following we use t ($t = 0, \ldots, N-1$) to denote a generic given time index, and i ($i = 1, \ldots, K$) to denote a generic given transmitter index.

MAMI-1 approximates the data model (1) as

$$\mathbf{y}_i(t) = \mathbf{a}(t)s_i(t) + \mathbf{e}_i(t), \tag{2}$$

where $\mathbf{y}_i(t) = [y_{i,1}(t), \ldots, y_{i,K}(t)]^T$ and $\mathbf{e}_i(t) = [e_{i,1}(t), \ldots, e_{i,K}(t)]^T$. The scalar $s_i(t)$ denotes the backscattered signal (from the focal point at location $\mathbf{r}$) corresponding to the

probing signal from the ith transmitting antenna. The vector $\mathbf{a}(t)$ in (2) is referred to as the array steering vector. Note that $\mathbf{a}(t)$ is approximately equal to $\mathbf{1}_{K \times 1}$ since all the signals have been aligned temporally and their attenuations compensated for in the preprocessing step.

There are three assumptions made to write the model in (2). First, the steering vector is assumed to vary with t, but be nearly constant with respect to i (the index of the transmitting antenna). Second, we assume that the backscattered signal waveform depends only on i but not on j (the index of the receiving antenna). The truth, however, is that the steering vector is not exactly known and it changes slightly with both t and i due to array calibration errors and other factors. The signal waveform can also vary slightly with both i and j, due to the (relatively insignificant) frequency-dependent lossy medium within the breast. The two aforementioned assumptions simplify the problem slightly. They cause little performance degradations when used with our robust adaptive algorithms. Third, we assume that the residual term is uncorrelated with the signal.

MAMI-2 approximates the data model (1) differently as follows:

$$\mathbf{y}_i(t) = \mathbf{a}_i s_i(t) + \mathbf{e}_i(t), \tag{3}$$

where $\mathbf{a}_i$ denotes the steering vector, which is again approximately $\mathbf{1}_{K \times 1}$. The second and third assumptions used to obtain (2) are also made to obtain (3). However, MAMI-2 assumes that the steering vector varies with i, but is constant with respect to t.

In practice, the steering vectors $\mathbf{a}(t)$ and $\mathbf{a}_i$ may be imprecise, in the sense that their elements may differ slightly from 1. This uncertainty in the steering vector motivates us to consider using RCB for waveform estimation. Because the steering vectors in (2) and (3) are both approximately $\mathbf{1}_{K \times 1}$, we assume that the true steering vector $\mathbf{a}(t)$ or $\mathbf{a}_i$ lies in uncertainty spheres, the centers of which are the assumed steering vector $\bar{\mathbf{a}} = \mathbf{1}_{K \times 1}$. (For the more general case of ellipsoidal uncertainty sets, see [19] and the references therein.) The only knowledge we assume about $\mathbf{a}(t)$ and $\mathbf{a}_i$ is, respectively, that

$$\begin{aligned} \left\| \mathbf{a}(t) - \bar{\mathbf{a}} \right\|^2 &\leq \epsilon_1, \\ \left\| \mathbf{a}_i - \bar{\mathbf{a}} \right\|^2 &\leq \epsilon_2, \end{aligned} \tag{4}$$

where ϵ_1 and ϵ_2 are used to describe the amount of uncertainty in $\mathbf{a}(t)$ and $\mathbf{a}_i$, respectively.

The choice of the uncertainty size parameters, ϵ_1 and ϵ_2, as well as of their counterparts in Stage II of MAMI-1 and MAMI-2 (see below), is determined by several factors such as the sample size N and the array calibration errors [17, 18]. First, they should be made as small as possible. Otherwise the ability of RCB to suppress an interference that is close to the signal of interest will be lost. Second, The smaller the N or the larger the steering vector errors, the larger should they be chosen. Third, to avoid trivial solution to the optimization problem of RCB, they should be less than the square of

the norm of the assumed steering vector [17, 18]. Such qualitative guidelines are usually sufficient for the choice of the uncertainty size parameters, since the performance of RCB does not depend very critically on them (as long as they take on "reasonable values") [19]. In our numerical examples, we choose certain reasonable initial values for them and then make some adjustments empirically based on imaging qualities (i.e., making them smaller when the current resulted images have low resolution or lots of clutter, or making them larger when the target in the current resulted images appears to be suppressed too).

3.   MAMI-1 AND MAMI-2

In Stage I, both MAMI-1 and MAMI-2 obtain K signal waveform estimates via RCB. In Stage I of MAMI-2, for the ith probing pulse, the true steering vector $\mathbf{a}_i$ can be estimated via the covariance fitting approach of RCB:

$$\max_{\sigma_i^2, \mathbf{a}_i} \sigma_i^2 \quad \text{subject to } \hat{\mathbf{R}}_{Y_i} - \sigma_i^2 \mathbf{a}_i \mathbf{a}_i^T \succeq 0, \; \|\mathbf{a}_i - \bar{\mathbf{a}}\|^2 \leq \epsilon_2, \tag{5}$$

where σ_i^2 is the power of the signal of interest, and

$$\hat{\mathbf{R}}_{Y_i} = \frac{1}{N} \mathbf{Y}_i \mathbf{Y}_i^T \tag{6}$$

is the sample covariance matrix with

$$\mathbf{Y}_i = [\mathbf{y}_i(0), \mathbf{y}_i(1), \ldots, \mathbf{y}_i(N-1)], \quad \mathbf{Y}_i \in \mathcal{R}^{K \times N}. \tag{7}$$

By using the Lagrange multiplier method, the solution to this optimization problem is given by [17]

$$\hat{\mathbf{a}}_i = \bar{\mathbf{a}} - [\mathbf{I} + \nu \hat{\mathbf{R}}_{Y_i}]^{-1} \bar{\mathbf{a}}, \tag{8}$$

where $\nu \geq 0$ is the corresponding Lagrange multiplier that can be solved efficiently from the following equation (e.g., using the Newton method):

$$\left\| (\mathbf{I} + \nu \hat{\mathbf{R}}_{Y_i})^{-1} \bar{\mathbf{a}} \right\|^2 = \epsilon, \tag{9}$$

since the left-hand side of (9) is monotonically decreasing in ν (see [17] for more details). After determining the multiplier ν, $\hat{\mathbf{a}}_i$ is determined by (8). To eliminate a scaling ambiguity (see [17]), we scale $\hat{\mathbf{a}}_i$ to make $\|\hat{\mathbf{a}}_i\|^2 = M$. Then we can apply the following weight vector to the received signals (see [17] for details):

$$\hat{\mathbf{w}}_{2,i} = \frac{\|\hat{\mathbf{a}}_i\|}{K^{1/2}} \cdot \frac{[\hat{\mathbf{R}}_{Y_i} + (1/\nu)\mathbf{I}]^{-1} \bar{\mathbf{a}}}{\bar{\mathbf{a}}^T [\hat{\mathbf{R}}_{Y_i} + (1/\nu)\mathbf{I}]^{-1} \hat{\mathbf{R}}_{Y_i} [\hat{\mathbf{R}}_{Y_i} + (1/\nu)\mathbf{I}]^{-1} \bar{\mathbf{a}}} \tag{10}$$

to obtain the corresponding signal waveform estimate. Note that (10) has a diagonal loading form, which can be used even when the sample covariance matrix is rank-deficient. The beamformer output can be written as the vector

$$\hat{\mathbf{s}}_i = [\hat{\mathbf{w}}_{2,i}^T \mathbf{Y}_i]^T, \quad \hat{\mathbf{s}}_i \in \mathcal{R}^{N \times 1}, \tag{11}$$

which is the waveform estimate of the backscattered signal (from the fixed location $\mathbf{r}$) for the ith probing signal. Repeating the above process for $i = 1$ through $i = K$, we obtain the complete set of K waveform estimates $\hat{\mathbf{S}}_2 = [\hat{\mathbf{s}}_1, \ldots, \hat{\mathbf{s}}_K]^T$, $\hat{\mathbf{S}}_2 \in \mathcal{R}^{K \times N}$.

Similarly, in Stage I of MAMI-1, we obtain a set of waveform estimates $\hat{\mathbf{S}}_1 = [\hat{\mathbf{s}}(0), \ldots, \hat{\mathbf{s}}(N-1)]$, $\hat{\mathbf{S}}_1 \in \mathcal{R}^{K \times N}$ (see [16] for details).

Note that Stage I of both MAMI-1 and MAMI-2 yields K waveform estimates of the backscattered signals (one for each transmitting antenna). Let $\{\hat{\mathbf{s}}_1(t)\}_{t=0,\ldots,N-1}$, and $\{\hat{\mathbf{s}}_2(t)\}_{t=0,\ldots,N-1}$ denote the columns of the matrices $\hat{\mathbf{S}}_1$ and $\hat{\mathbf{S}}_2$, respectively. Since all probing signals have the same waveform, we assume that the true backscattered signal waveforms are (nearly) identical. This means that, for example, for MAMI-2, the elements of the vector $\hat{\mathbf{s}}_2(t)$ are all approximately equal to an unknown (scalar) signal $s(t)$. So in Stage II, we can employ RCB to recover a scalar waveform $\hat{s}(t)$ from $\{\hat{\mathbf{s}}_1(t)\}$ or $\{\hat{\mathbf{s}}_2(t)\}$ (see [16] for more details on Stage II of MAMI-1; Stage II of MAMI-2 is similar). Finally, the backscattered energy $E(\mathbf{r})$ is computed as

$$E(\mathbf{r}) = \sum_{t=0}^{N-1} \hat{s}^2(t). \tag{12}$$

It is well known that the errors in sample covariance matrices (e.g., the $\hat{\mathbf{R}}_{Y_i}$ above) and the steering vectors cause performance degradations in adaptive beamforming [22, 23]. Note that, on one hand, MAMI-2 uses more snapshots (namely, N) than MAMI-1 (namely, K) to estimate the sample covariance matrix. Therefore, the sample covariance matrix of MAMI-2 is more precise than that of MAMI-1. On the other hand, MAMI-1 employs RCB N times, whereas MAMI-2 uses RCB K times (recall that $N > K$), so there is more "room" for robustness in MAMI-1 than in MAMI-2, which means that MAMI-1 should be more robust to steering vector errors. In summary, MAMI-2 uses a more precise sample covariance matrix, whereas MAMI-1 is more robust against steering vector mismatch. Therefore, according to what was said above, at high input SINR (when the sample covariance matrix errors are more important) we can expect MAMI-2 to perform better than MAMI-1, and vice versa at low input SINR (when the errors in the steering vector are critical).

4.   MAMI-C

The previous intuitive discussions on MAMI-1 and MAMI-2 and the numerical examples presented later on imply that

MAMI-2 has better performance at high SINR, while MAMI-1 usually outperforms MAMI-2 at low SINR. This fact motivates us to consider combining MAMI-1 and MAMI-2 to achieve good performance in all cases of SINR. In the combined method, which is referred to as MAMI-C, we use the two sets of K waveform estimates yielded by Stage I of MAMI-1 and Stage I of MAMI-2 simultaneously in Stage II (note that MAMI-1 and MAMI-2 have a similar Stage II). In this way the combined method increases the number of "fictitious" array elements from K to $2K$.

The combined set of estimated waveforms is denoted by $\hat{\mathbf{S}}_C = [\hat{\mathbf{s}}_1^T \ \hat{\mathbf{s}}_2^T]^T$, $\hat{\mathbf{S}}_C \in \mathcal{R}^{2K \times N}$, where the subscript $(\cdot)_C$ stands for MAMI-C. Let the $2K \times 1$ vectors $\{\hat{\mathbf{s}}(t)\}_{t=0,\dots,N-1}$ denote the columns of $\hat{\mathbf{S}}_C$. Stage II of MAMI-C consists of recovering a scalar waveform from $\{\hat{\mathbf{s}}(t)\}$.

The vector $\hat{\mathbf{s}}(t)$ is treated as a snapshot from a $2K$-element (fictitious) "array":

$$\hat{\mathbf{s}}(t) = \mathbf{a}_C s(t) + \mathbf{e}_C(t), \quad t = 0,\dots,N-1, \qquad (13)$$

where $\mathbf{a}_C$ is assumed to belong to an uncertainty set centered at $\tilde{\mathbf{a}} = \mathbf{1}_{2K \times 1}$, and $\mathbf{e}_C(t)$ represents the estimation error. Using RCB, we estimate $\mathbf{a}_C$ and then obtain the adaptive weight vector via an expression similar to (10):

$$\hat{\mathbf{w}}_C = \frac{\|\hat{\mathbf{a}}_C\|}{K^{1/2}} \cdot \frac{(\hat{\mathbf{R}}_C + (1/\mu)\mathbf{I})^{-1}\tilde{\mathbf{a}}}{\tilde{\mathbf{a}}^T(\hat{\mathbf{R}}_C + (1/\mu)\mathbf{I})^{-1}\hat{\mathbf{R}}_C(\hat{\mathbf{R}}_C + (1/\mu)\mathbf{I})^{-1}\tilde{\mathbf{a}}}, \qquad (14)$$

where μ is the corresponding Lagrange multiplier (see [17] for more details), and $\hat{\mathbf{R}}_C$ is the following sample covariance matrix:

$$\hat{\mathbf{R}}_C = \frac{1}{N}\sum_{t=0}^{N-1} \hat{\mathbf{s}}(t)\hat{\mathbf{s}}^T(t). \qquad (15)$$

The beamformer output gives an estimate of the signal of interest:

$$\hat{s}(t) = \hat{\mathbf{w}}_C^T \hat{\mathbf{s}}(t). \qquad (16)$$

Finally, the backscattered energy at location $\mathbf{r}$ is computed using (12).

Remark 1. It is natural to come up with a third way of slicing the data cube in Stage I before applying RCB: to select a slice corresponding to each receiving antenna index (see Figure 2). Our numerical examples show that the performance of this method is similar to that of MAMI-2. Moreover, we can use the waveform estimates from this approach together with those estimated in Stage I of MAMI-1 and

Stage I of MAMI-2 to estimate a scalar waveform. However, numerical examples show that such a combination provides no significant improvement over MAMI-C, but the computational complexities increase due to the increased data dimension in Stage II. Therefore, we will not consider this option any further hereafter.

5. NUMERICAL EXAMPLES

We consider a 3D breast model as in [16] in our numerical examples. The model includes randomly distributed fatty breast tissue, glandular tissue, 2 mm-thick breast skin, as well as the nipple and chest wall. To reduce the reflections from the breast skin, the breast model is immersed in a lossless liquid with permittivity similar to that of the breast fatty tissue [24]. The breast model is a hemisphere with 10 cm in diameter. A tumor that is 6 mm (or 4 mm) in diameter is located 2.7 cm under the skin (at $x = 70$ mm, $y = 90$ mm, $z = 60$ mm). Two cross-sections of the 3D model are shown in Figure 3.
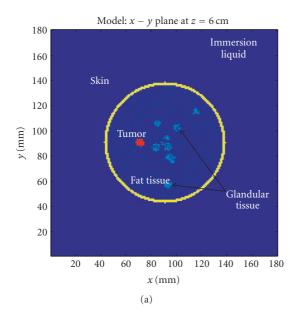
We assume that the dielectric properties (permittivity and conductivity) of the breast tissues are Gaussian random variables with a mean equal to their nominal values and a variance equal to 0.1 times their mean values. This variation represents an upper bound on reported breast tissue variabilities [4, 5]. The nominal values are chosen to be the typical values reported in the literature [3–7], as shown in Table 1. Since UWB pulses are used as probing signals, the dispersive properties of the fatty breast tissue and those of the tumor are also considered in the model. The frequency dependencies of the permittivity $\varepsilon(\omega)$ and conductivity $\sigma(\omega)$ are modelled according to a single-pole Debye model [8]. The randomly distributed breast tissues with variable dielectric properties represent the physical nonhomogeneity of the human breast.
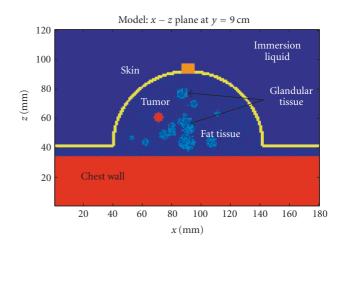
As shown in Figure 1, the antenna array consists of $K = 72$ elements that are arranged on a hemisphere, which is 1 cm away from the breast skin, on $P = 6$ layers in the z-axis dimension. The layers of antennas are arranged along the z-axis between 5.0 cm and 7.5 cm, with 0.5 cm spacing. Within each layer, $Q = 12$ antennas are placed on a cross-sectional circle with uniform spacing. The UWB signal used is a Gaussian pulse given by

$$G(t) = \exp\left\{-\left(\frac{t - \tau_0}{\tau}\right)^2\right\}, \qquad (17)$$

where $\tau_0 = 25\,\mu$s, $\tau = 10\,\mu$s, and the pulse width is roughly 120 ps. Each antenna of the array takes turns to transmit the Gaussian probing pulse, and all 72 antennas are used to receive the backscattered signals.

FDTD [25, 26] is used to obtain the simulated data. The grid cell size used is 1 mm $\times$ 1 mm $\times$ 1 mm and the time step is 1.667 ps. The model is terminated according to perfectly matched layer absorbing boundary conditions [27]. The Z-transform [28] is used to implement the FDTD method whenever materials with frequency-dependent properties are

FIGURE 3: Cross-sections of a 3D hemispherical breast model at (a) $z = 60$ mm and (b) $y = 90$ mm.

involved. Finally, the time window in the preprocessing step consists of 150 samples, which means that $N = 150$ for each of the preprocessed signals.

The performance comparisons of MAMI-1 with other existing methods can be found in [16]. In the following, we focus on comparing MAMI-1 with the other two MAMI methods.

In the following examples, we add white Gaussian noise with zero-mean and different variance values σ_0^2 to the received signals. We define SNR (signal-to-noise ratio) as

$$\text{SNR} = 10 \log_{10}$$

$$\times \left\{ \frac{(1/K^2) \sum_{i=1}^{K} \sum_{j=1}^{K} \left[(1/N) \sum_{t=0}^{N-1} \check{x}_{i,j}^2(t) \right]}{\sigma_0^2} \right\} \text{dB},$$

$$(18)$$

and SINR as

$$\text{SINR} = 10 \log_{10}$$

$$\times \left\{ \frac{(1/K^2) \sum_{i=1}^{K} \sum_{j=1}^{K} \left[(1/N) \sum_{t=0}^{N-1} \check{x}_{i,j}^2(t) \right]}{(1/K^2) \sum_{i=1}^{K} \sum_{j=1}^{K} \left[(1/N) \sum_{t=0}^{N-1} \check{I}_{i,j}^2(t) \right] + \sigma_0^2} \right\} \text{dB}.$$

$$(19)$$

The $\check{x}_{i,j}(t)$ in (19) is the received signal due to the tumor only, and $\check{I}_{i,j}(t)$ is due to the interference from breast skin, nipple, and so forth (without tumor response), both of which are not available in practice. To compute SNR and SINR, we performed the simulation twice, with and without the tumor, regarded the second set of received signals as interference only,

TABLE 1: Nominal dielectric properties of breast tissues.

Tissues	Dielectric properties	
	Permittivity (F/m)	Conductivity (S/m)
Immersion liquid	9	0
Chest wall	50	7
Skin	36	4
Fatty breast tissue	9	0.4
Nipple	45	5
Glandular tissue	11–15	0.4–0.5
Tumor	50	4

and used the difference between the two sets of received signals to approximate $\check{x}_{i,j}(t)$. All the images are displayed on a logarithmic scale with a dynamic range of 40 dB (note that here the dynamic range used is larger than the 20 dB dynamic range in [16]).

Figures 4 and 5 show the CMI images of a 6 mm-diameter tumor, at low and high thermal noise levels, respectively. At the low noise level (SNR = 12.1 dB, SINR = −1.4 dB), the images produced by MAMI-2 have much more focused tumor responses than those of MAMI-1. The images of MAMI-C have similar qualities to those of MAMI-2. In Figure 5, at the high noise level (SNR = −13.8 dB, SINR = −14.1 dB), MAMI-1 yields better images than MAMI-2, and that MAMI-C is slightly better than MAMI-1. This example demonstrates that MAMI-C inherits the merits of both MAMI-1 and MAMI-2.

Figures 6 and 7 show the images of a 4 mm-diameter tumor with different thermal noise levels. The backscattered microwave energy, which is proportional to the square of the tumor diameter, is much less in this case than in the previous
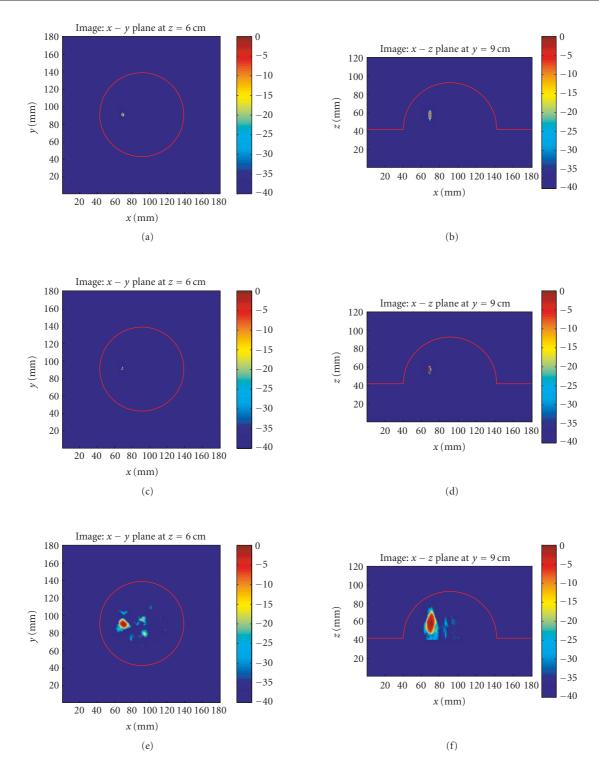
FIGURE 4: The cross-section images of the 6 mm-diameter tumor, at low noise level (SNR = 12.1 dB, SINR = −1.4 dB). (a) and (b) MAMI-C; (c) and (d) MAMI-2 with $\epsilon_2 = 7$; (e) and (f) MAMI-1 with $\epsilon_1 = 3$. (In all of our examples, the given ϵ_2 and ϵ_1 are used for both stages.)

example. That is, if the thermal noise level is kept the same as in the 6 mm-diameter tumor case, both the SNR and SINR will be much lower in the 4 mm-diameter case, which presents a challenge to any image formation algorithm. In Figure 6, at a low noise level (SNR = 1.5 dB, SINR = −12.5 dB),

MAMI-2 and MAMI-C yield images of comparable qualities and they outperform MAMI-1. Figure 7 shows the images produced via the MAMI methods at a high noise level (SNR = −24.5 dB, SINR = −24.8 dB). Once again, MAMI-C yields the best images.
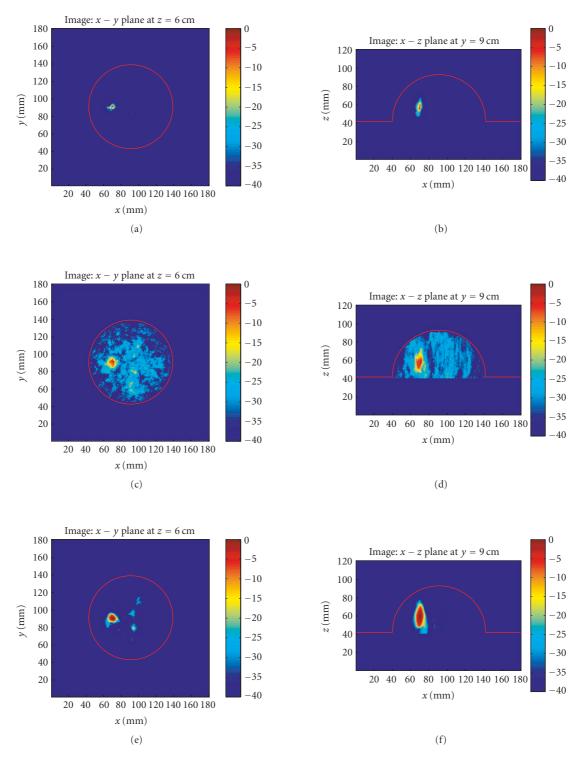
(a)

(b)

(c)

(d)

(e)

(f)

FIGURE 5: The cross-section images of the 6 mm-diameter tumor, at high noise level (SNR $= -13.8$ dB, SINR $= -14.1$ dB). (a) and (b) MAMI-C; (c) and (d) MAMI-2 with $\epsilon_2 = 7$; (e) and (f) MAMI-1 with $\epsilon_1 = 3$.

Finally, **Figure 8** presents the 3D images of the 6 mm- as well as the 4 mm-diameter tumor. The 3D images, although not as clear visually as the cross-sectional images, illustrate the reconstructed backscattered energy outside the two cross-sectional planes. Here we only show the 3D images for the low-noise-level cases. In these figures the true tumor locations are marked with small "+"s. In Figures 8(a) and 8(d), which correspond to the images produced by MAMI-C,
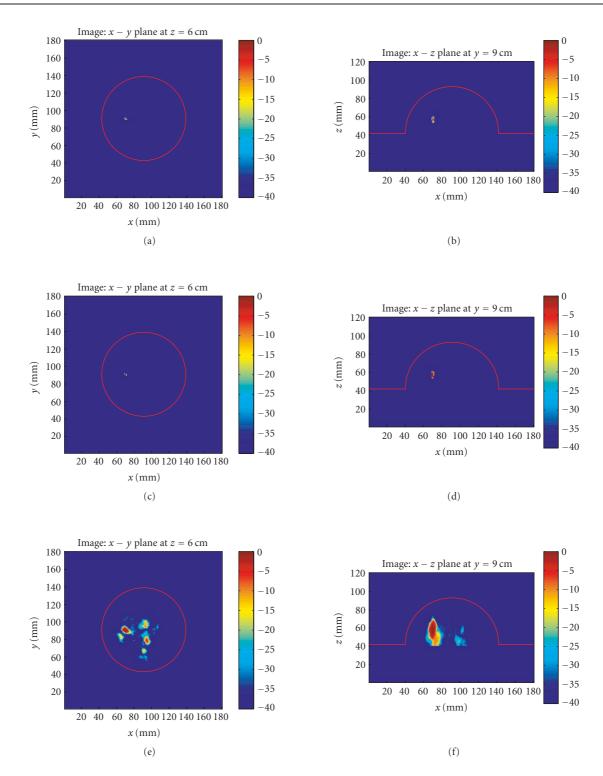
(a)

(b)

(c)

(d)

(e)

(f)

FIGURE 6: The images of the 4 mm-diameter tumor, at low noise level (SNR = 1.5 dB, SINR = −12.5 dB). (a) and (b) MAMI-C; (c) and (d) MAMI-2 with $\epsilon_S = 8.5$; (e) and (f) MAMI-1 with $\epsilon_M = 5$.

and in 8(b) and 8(e), which correspond to the images produced by MAMI-2, besides the tumor responses, no clutter is clearly visible. Figures 8(c) and 8(f) show the MAMI-1 images; particularly in the latter image, clutter abounds within the breast volume.

6. CONCLUSIONS

We have presented and compared several multistatic adaptive microwave imaging (MAMI) methods for early breast cancer detection. The MAMI methods utilize the data-adaptive
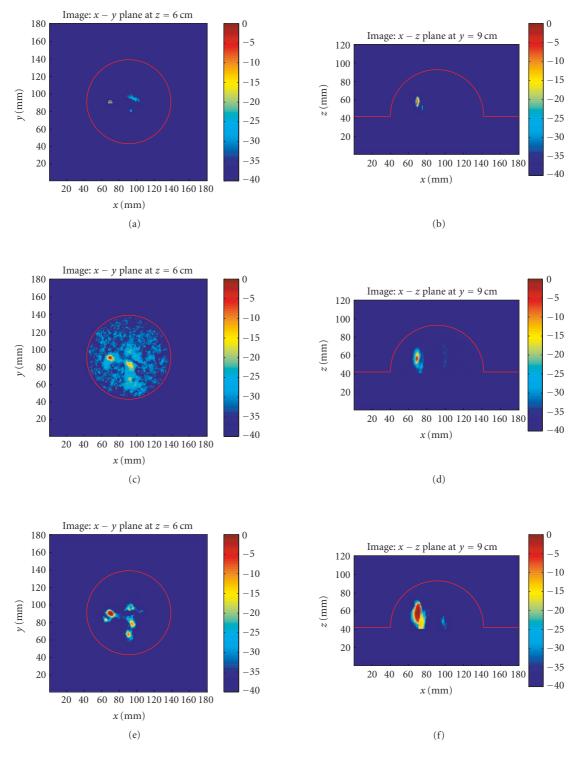
(a)

(b)

(c)

(d)

(e)

(f)

FIGURE 7: The images of the 4 mm-diameter tumor, at high noise level (SNR $= -24.5$ dB, SINR $= -24.8$ dB). (a) and (b) MAMI-C; (c) and (d) MAMI-2 with $\epsilon_2 = 8.5$; (e) and (f) MAMI-1 with $\epsilon_1 = 5$.

robust Capon beamformer (RCB) to achieve high resolution and interference suppression. We have demonstrated the effectiveness of the MAMI methods for early breast cancer detection via numerical examples with data simulated using the finite difference time domain method based on a 3D realistic breast model. We have shown that the MAMI-C method can detect tumors as small as 4 mm in diameter based on the realistically simulated 3D breast model.
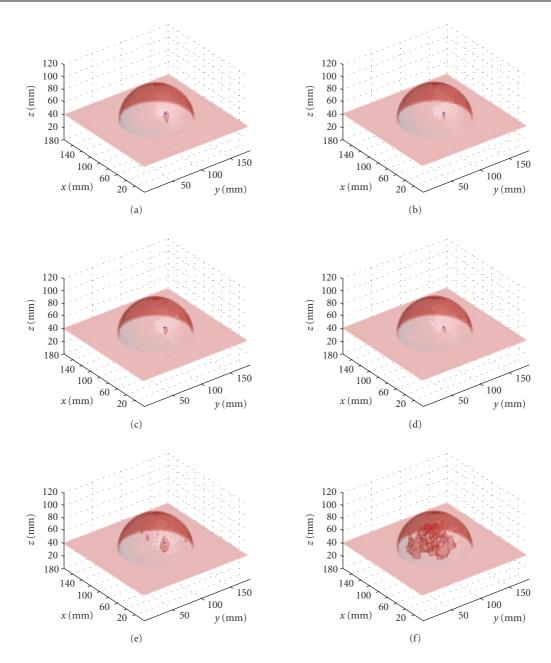
(a)

(b)

(c)

(d)

(e)

(f)

FIGURE 8: The 3D images of the 6 mm-diameter tumor, at low noise level (SNR = 12.1 dB, SINR = −1.4 dB), obtained via (a) MAMI-C, (c) MAMI-2, (e) MAMI-1. Also, the 3D images of the 4 mm-diameter tumor, at low noise level (SNR = 1.5 dB, SINR = −12.5 dB), obtained via (b) MAMI-C, (d) MAMI-2, (f) MAMI-1. The shaded hemisphere is the contour of the breast, and the dotted shades within the breast correspond to high backscattered energy. The small "+" marks the true location of the tumor.

REFERENCES

[1] S. J. Nass, I. C. Henderson, and J. C. Lashof, *Mammography and Beyond: Developing Techniques for the Early Detection of Breast Cancer*, Institute of Medicine, National Academy Press, Washington, DC, USA, 2001.

[2] E. C. Fear, S. C. Hagness, P. M. Meaney, M. Okoniewski, and M. A. Stuchly, "Enhancing breast tumor detection with near-field imaging," *IEEE Microwave Magazine*, vol. 3, no. 1, pp. 48–56, 2002.

[3] C. Gabriel, R. W. Lau, and S. Gabriel, "The dielectric properties of biological tissues: II. Measurements in the frequency range 10 Hz to 20 GHz," *Physics in Medicine and Biology*, vol. 41, no. 11, pp. 2251–2269, 1996.

[4] S. S. Chaudhary, R. K. Mishra, A. Swarup, and J. M. Thomas, "Dielectric properties of normal and malignant human breast tissues at radiowave and microwave frequencies," *Indian Journal of Biochemistry and Biophysics*, vol. 21, pp. 76–79, 1984.

[5] W. T. Joines, Y. Zhang, C. Li, and R. L. Jirtel, "The measured electrical properties of normal and malignant human tissues from 50 to 900 MHz," *Medical Physics*, vol. 21, no. 4, pp. 547–550, 1994.

[6] A. J. Surowiec, S. S. Stuchly, J. R. Barr, and A. Swarup, "Dielectric properties of breast carcinoma and the surrounding tissues," *IEEE Transactions on Biomedical Engineering*, vol. 35, no. 4, pp. 257–263, 1988.

[7] A. Swarup, S. S. Stuchly, and A. J. Surowiec, "Dielectric properties of mouse MCA1 fibrosarcoma at different stages of development," *Bioelectromagnetics*, vol. 12, no. 1, pp. 1–8, 1991.

[8] X. Li and S. C. Hagness, "A confocal microwave imaging algorithm for breast cancer detection," *IEEE Microwave and Wireless Components Letters*, vol. 11, no. 3, pp. 130–132, 2001.

[9] B. Guo, Y. Wang, J. Li, P. Stoica, and R. Wu, "Microwave imaging via adaptive beamforming methods for breast cancer detection," in *Proceedings of Progress in Electromagnetics Research Symposium (PIERS '05)*, Hangzhou, China, August 2005.

[10] B. Guo, Y. Wang, J. Li, P. Stoica, and R. Wu, "Microwave imaging via adaptive beamforming methods for breast cancer detection," *Journal of Electromagnetic Waves and Applications*, vol. 20, no. 1, pp. 53–63, 2006.

[11] R. Nilavalan, A. Gbedemah, I. J. Craddock, X. Li, and S. C. Hagness, "Numerical investigation of breast tumour detection using multi-static radar," *IEE Electronics Letters*, vol. 39, no. 25, pp. 1787–1789, 2003.

[12] E. Fishler, A. Haimovich, R. Blum, D. Chizhik, L. Cimini, and R. Valenzuela, "MIMO radar: an idea whose time has come," in *Proceedings of IEEE Radar Conference*, pp. 71–78, Philadelphia, Pa, USA, April 2004.

[13] E. Fishler, A. Haimovich, R. Blum, D. Chizhik, L. Cimini, and R. Valenzuela, "Spatial diversity in radars—models and detection performance," to appear in *IEEE Transactions on Signal Processing*.

[14] L. Xu, J. Li, and P. Stoica, "Radar Imaging via Adaptive MIMO Techniques," in *Proceedings of 14th European Signal Processing Conference (EUSIPCO '06)*, Florence, Italy, September 2006, ftp://www.sal.ufl.edu/xuluzhou/EUSIPCO2006.pdf.

[15] E. J. Bond, X. Li, S. C. Hagness, and B. D. Van Veen, "Microwave imaging via space-time beamforming for early detection of breast cancer," *IEEE Transactions on Antennas and Propagation*, vol. 51, no. 8, pp. 1690–1705, 2003.

[16] Y. Xie, B. Guo, L. Xu, J. Li, and P. Stoica, "Multi-static adaptive microwave imaging for early breast cancer detection," in *Proceedings of 39th ASILOMAR Conference on Signals, Systems and Computers*, Pacific Grove, Calif, USA, October 2005.

[17] J. Li, P. Stoica, and Z. Wang, "On robust Capon beamforming and diagonal loading," *IEEE Transactions on Signal Processing*, vol. 51, no. 7, pp. 1702–1715, 2003.

[18] P. Stoica, Z. Wang, and J. Li, "Robust Capon beamforming," *IEEE Signal Processing Letters*, vol. 10, no. 6, pp. 172–175, 2003.

[19] J. Li and P. Stoica, Eds., *Robust Adaptive Beamforming*, John Wiley & Sons, New York, NY, USA, 2005.

[20] E. C. Fear, X. Li, S. C. Hagness, and M. A. Stuchly, "Confocal microwave imaging for breast cancer detection: localization of tumors in three dimensions," *IEEE Transactions on Biomedical Engineering*, vol. 49, no. 8, pp. 812–822, 2002.

[21] E. C. Fear and M. Okoniewski, "Confocal microwave imaging for breast cancer detection: Application to hemispherical breast model," in *Proceedings of IEEE MTT-S International Microwave Symposium Digest*, vol. 3, pp. 1759–1762, Seattle, Wash, USA, June 2002.

[22] R. A. Monzingo and T. W. Miller, *Introduction to Adaptive Arrays*, John Wiley & Sons, New York, NY, USA, 1980.

[23] D. D. Feldman and L. J. Griffiths, "A projection approach for robust adaptive beamforming," *IEEE Transactions on Signal Processing*, vol. 42, no. 4, pp. 867–876, 1994.

[24] P. M. Meaney, "Importance of using a reduced contrast coupling medium in 2D microwave breast imaging," *Journal of Electromagnetic Waves and Applications*, vol. 17, no. 2, pp. 333–355, 2003.

[25] D. M. Sullivan, *Electromagnetic Simulation Using FDTD Method*, Wiley/IEEE Press, New York, NY, USA, 1st edition, 2000.

[26] A. Taflove and S. C. Hagness, *Computational Electrodynamics: The Finite-Difference Time-Domain Method*, Artech House, Boston, Mass, USA, 3rd edition, 2005.

[27] S. D. Gedney, "An anisotropic perfectly matched layer-absorbing medium for the truncation of FDTD lattices," *IEEE Transactions on Antennas and Propagation*, vol. 44, no. 12, pp. 1630–1639, 1996.

[28] D. M. Sullivan, "Z-transform theory and the FDTD method," *IEEE Transactions on Antennas and Propagation*, vol. 44, no. 1, pp. 28–34, 1996.

Yao Xie received the B.S. degree in electrical engineering and information science from the University of Science and Technology of China (USTC), Hefei, China, in 2004. She is currently pursuing the Ph.D. degree with the Department of Electrical and Computer Engineering at the University of Florida, Gainesville. She is a Member of Tau Beta Pi and Etta Kappa Nu. She was the first-place winner in the Student Best Paper Contest at the 2005 Annual Asilomar Conference on Signals, Systems, and Computers, for her work on breast cancer detection. Her research interests include signal processing, medical imaging, and array signal processing.

Bin Guo received the B.E. and M.S. degrees in electrical engineering from Xian Jiaotong University, Xian, China, in 1997 and 2000, respectively. From April 2002 to July 2003, he was an Associate Research Scientist with the Temasek Laboratories, National University of Singapore, Singapore. Since August 2003, he has been a Research Assistant with the Department of Electrical and Computer Engineering, University of Florida, Gainesville, where he is pursuing the Ph.D. degree in electrical engineering. His current research interests include biomedical applications of signal processing, microwave imaging, and computational electromagnetics.

Jian Li received the M.S. and Ph.D. degrees in electrical engineering from the Ohio State University, Columbus, in 1987 and 1991, respectively. From July 1991 to June 1993, she was an Assistant Professor with the Department of Electrical Engineering, University of Kentucky, Lexington. Since August 1993, she has been with the Department of Electrical and Computer Engineering, University of Florida, Gainesville, where she is currently a Professor. Her current research interests include spectral estimation, statistical and array signal processing,

and their applications. Dr. Li is a Fellow of IEEE and a Fellow of IEE. She received the 1994 National Science Foundation Young Investigator Award and the 1996 Office of Naval Research Young Investigator Award. She has been a Member of the Editorial Board of Signal Processing, a publication of the European Association for Signal Processing (EURASIP), since 2005. She is presently a Member of two of the IEEE Signal Processing Society technical committees: the Signal Processing Theory and Methods (SPTM) Technical Committee and the Sensor Array and Multichannel (SAM) Technical Committee.

Petre Stoica received the M.S. and Ph.D. degrees in automatic control from the Polytechnic Institute of Bucharest, Bucharest, Romania, in 1972 and 1979, respectively. He is currently a Professor of system modeling at Uppsala University, Uppsala, Sweden. Other details about him are available at http://user.it.uu.se/~ps/ps.html.